Journal of Materiomics 11 (2025) 100932

Contents lists available at ScienceDirect

Journal of Materiomics

journal homepage: www.journals.elsevier.com/journal-of-materiomics/

Research paper

Advancement in PMN-PT transparent piezoelectric ceramic for photoacoustic/ultrasound dual-mode imaging

Pengkun Guo [a, 1], Wen Gao [a, 1], Riqiang Lin [b, 1], Xiatian Wang [b], Jiale Lan [b], Jiaming Zhang [d], Yanan Wang [a], Lin Zhu [a], Yongcheng Zhang [a], Feng Li [e], Weijie Zheng [a], Tianlong Zhao [f], Kwok-Ho Lam [d], Xiaojing Gong [b, **], Zhihua Xie [b, ***], Yalin Qin [a, *], Shujun Zhang [c]

[a] College of Physics, National Demonstration Center for Experimental Applied Physics Education, Qingdao University, Qingdao, 266071, Shandong, China
[b] Research Center for Biomedical Optics and Molecular Imaging, Key Laboratory of Biomedical Imaging Science and System, Shenzhen Institute of Advanced Technology, Chinese Academy of Sciences, Shenzhen, 518055, Guangdong, China
[c] Institute for Superconductor and Electronic Materials, Faculty of Engineering and Information Sciences, University of Wollongong, Wollongong, NSW, 2500, Australia
[d] Department of Electrical and Electronic Engineering, The Hong Kong Polytechnic University, Hung Hom, Kowloon, Hong Kong, SAR, China
[e] Institutes of Physical Science and Information Technology, Anhui University, Hefei, 230601, China
[f] School of Microelectronics, Xidian University, Xi'an, 710071, China

A R T I C L E I N F O

Article history:
Received 14 May 2024
Received in revised form
26 July 2024
Accepted 7 August 2024
Available online 30 August 2024

Keywords:
PMN-PT
Transparent ceramics
Transparent piezoelectric ultrasonic transducer
Photoacoustic/ultrasound dual-mode imaging
Photoacoustic imaging

A B S T R A C T

Dual-mode imaging combining photoacoustic and ultrasound modalities holds great promise for comprehensive tissue characterization. In traditional dual-mode imaging systems, however, the opaque ultrasound transducers are integrated in complex optical and ultrasound paths, leading to compromises in imaging efficiency and sensitivity. To address these challenges, we design and produce highly transparent $Pb(Mg,Nb)O_3{-}PbTiO_3$ ceramics with exceptional transparency of 68%, alongside a remarkable ultrahigh piezoelectric d_{33} of 1500 pC/N. Leveraging this material, we fabricate a high-sensitivity transparent piezoelectric ultrasound transducer (TPUT) with a center frequency of 16 MHz and a bandwidth of 30%, which seamlessly integrating ultrasound and photoacoustic capabilities into one system to achieve simultaneous photoacoustic/ultrasound dual-mode imaging, showcasing a remarkable sensitivity for deep-tissue detection (*e.g.*, 7.5 mm thick chicken breast meat). Additionally, *in vivo* photoacoustic imaging of subcutaneous microvasculature in a mouse ear was successfully achieved *via* 28 MHz TPUT. Our innovation not only advances imaging performance but also offers a cost-effective solution, paving the way for transformative biomedical imaging applications.
© 2024 The Authors. Published by Elsevier B.V. on behalf of The Chinese Ceramic Society. This is an open access article under the CC BY-NC-ND license (http://creativecommons.org/licenses/by-nc-nd/4.0/).

1. Introduction

Photoacoustic (PA) imaging is a hybrid modality, holding the advantages of high imaging contrast and depth penetration. In PA imaging, the bio-tissues absorb diffused photons and generate photoacoustic signals, which is subsequently detected by ultrasound transducer. This process allows for differentiation and quantification of tissue components, offering valuable functional information of tissues. Generally speaking, the PA imaging is often coupled with ultrasound (US) imaging, providing complementary functional and structural information simultaneously. The PA/US dual-mode imaging combines the high optical resolution of PA with the deep penetration of US, improving the accuracy of medical diagnosis as well as therapeutic monitoring. The development of PA/US dual-mode imaging technology is currently a focal point in the field [1–4].

Traditionally, PA/US imaging systems utilizes opaque piezoelectric ultrasound transducers for ultrasound signal emission and detection, where the complex optical design, such as multiple light reflection or annular light shaping, is mandatory to mitigate the influence of opaque transducer in PA imaging. These designs often result in extended working distance and ultrasound signal

* Corresponding author.
** Corresponding author.
*** Corresponding author.
E-mail addresses: xj.gong@siat.ac.cn (X. Gong), xie@siat.ac.cn (Z. Xie), yalinqin@qdu.edu.cn (Y. Qin).
Peer review under responsibility of The Chinese Ceramic Society.
[1] These authors contribute equally to this article: P. Guo, W. Gao, R. Lin.

https://doi.org/10.1016/j.jmat.2024.100932
2352-8478/© 2024 The Authors. Published by Elsevier B.V. on behalf of The Chinese Ceramic Society. This is an open access article under the CC BY-NC-ND license (http://creativecommons.org/licenses/by-nc-nd/4.0/).

attenuation, reducing the imaging efficiency and limiting the imaging resolution [5–9]. Although center-drilled (annular) piezoelectric ultrasound transducers offers the advantage of allowing laser beams to pass through unhindered and facilitating concentric alignment of light and sound beams, they suffer from decreased detection efficiency and sacrificed imaging sensitivity [10]. All above challenges will find solutions if the ultrasound transducers become transparent, in which the light will propagate through the transducer directly and the imaging distance will be optimized to achieve a higher imaging efficiency.

In the PA/US dual-mode imaging applications with transparent piezoelectric ultrasound transducers (TPUT), high transparency and good piezoelectric performance of the transducer are necessary to ensure the efficient laser penetration for photoacoustic excitation and the high efficiency of ultrasound detection, respectively. However, piezoelectric materials with both high transparency and good piezoelectric properties are scarce. To date, polyvinylidene fluoride (PVDF) films, transparent $LiNbO_3$ (abbreviated as LN) single crystals, and $Pb(Mg_{1/3}Nb_{2/3})O_3$–$PbTiO_3$ (abbreviated as PMN-PT) single crystals have been used to fabricate TPUTs for PA imaging or PA/US dual-mode imaging [11–14]. In 2005, M. Frenz *et al.* [15] reported a transparent ITO coated PVDF transducer which can provide transparency for the illuminating laser beam in backward mode (the laser illumination and acoustic sensing are on the same side) and reduce acoustic diffraction artifacts using large area irradiation. PVDF, renowned for its good flexibility and high detection sensitivity, continues to be a fundamental element in PA imaging [11–13,16,17]. In 2014, Graham W.J. Brodie *et al.* [18] highlighted the superiority of LN TPUTs over PVDF transducer, enabling simultaneous PA and US imaging and broadening the scope of hybrid ultrasonic–optical systems. In 2019, Ajay Dangi *et al.* [19] pioneered the application of LN TPUT in PA imaging, achieving successful imaging of phantoms. Despite exhibiting excellent optical transparency (T ~ 80%) in visible and near infrared wavelengths, both PVDF [20,21]and LN [22] suffer from inferior piezoelectric and electromechanical performance (d_{33} < 40 pC/N, k_{33} < 50%), hindering their efficacy in US imaging and limiting the advancement of PA/US dual-mode imaging quality. Between 2020 and 2023, alternating current (AC)-poled PMN-PT single crystals [23], with both excellent piezoelectric coefficients (d_{33} > 2100 pC/N) and high transparency (T ~ 70%), were applied in TPUT, showcasing superior ultrasound imaging quality and signal-to-noise ratio (SNR) in PA/US dual-mode imaging [14,24,25]. However, the high production costs, delicate fabrication processes, and complex device processing associated with single crystals, inevitably increases the difficulty and cost of their commercial application. Although ceramic materials hold promise in addressing these issues, the preparation of transparent piezoelectric ceramics remains challenging due to the light scattering on the ferroelectric domain walls, grain boundaries and pores *etc.* Consequently, transparent piezoelectric ceramics have yet to be leveraged for TPUT. Therefore, identifying ceramic materials with both high transparency and superior piezoelectric properties for TPUT, the key component in PA imaging or PA/US dual-mode imaging, is of great importance in reducing the cost for commercial applications.

In recent years, considerable efforts have been devoted to develop highly transparent piezoelectric ceramics across different systems, such as $(K,Na)NbO_3$ (abbreviated as KNN), $BaTiO_3$ (abbreviated as BT), PMN-PT based ceramics, among others. KNN based ceramics show relatively high transmittance around 70% [26–33], yet their d_{33} generally doesn't exceed 200 pC/N. The fine-grained BT ceramics prepared by hot pressing method have high piezoelectric properties (d_{33} ~ 420 pC/N) and average transparency (T ~ 40% @900 nm) [34]. Recently, a 2.5% (in mole) Eu doped PMN-28PT transparent ceramic was report to exhibit both high piezoelectric properties and transparency by domain engineering method, with d_{33} ~ 1400 pC/N and T ~ 68% @ 900 nm [35]. Its comprehensive performance ranks second only to AC-poled PMN-PT single crystal and surpasses other transparent piezoelectric ceramics, rendering it a suitable ceramic material for TPUT fabrication.

In this work, a 2% (in mole) Eu^{3+} doped PMN-28PT (abbreviated as 2%Eu-PMN-28PT) transparent ceramics (T ~ 68% @900 nm) with an even higher piezoelectric coefficient d_{33} up to 1500 pC/N was prepared. Employing this transparent piezoelectric ceramic, we developed a high-sensitivity TPUT featuring a center frequency of 16 MHz and a bandwidth of 30%. Integrating both PA and US imaging modalities, we successfully acquired two-mode images of the phantoms. Notably, we were able to capture PA/US signals from the targets located 7.5 mm beneath chicken breast tissue, maintaining a high PA's SNR at 21 dB, demonstrating the impressive sensitivity of the designed TPUT. Additionally, *in vivo* photoacoustic imaging of subcutaneous microvasculature in a mouse ear has also been carried out by a 28 MHz TPUT, showcasing great advantages of the transparent high performance ceramics.

2. Experimental section

2.1. Preparation of ceramics

We prepared the 0.98[0.72 $Pb(Mg_{1/3}Nb_{2/3})O_3$-0.28$PbTiO_3$]-0.02Eu_2O_3 (2%Eu-PMN-28PT) ceramic using a two-step sintering process, including oxygen sintering and hot-press sintering. The high-purity Nb_2O_5 (99.99%, Aladdin), MgO (99.99%, Aladdin), PbO (99.99%, Aladdin), TiO_2 (99.99%, Aladdin), and Eu_2O_3 (99.99%, Aladdin) powders were used as raw materials. For detailed sintering procedures, please refer to our previously published work [36].

2.2. Fabrication of TPUT

Fig. 1 shows the manufacturing steps of TPUT: (1) A transparent PMN-PT ceramic wafer with a diameter of 10 mm and thickness of 150 μm and 80 μm was prepared; (2) Deposit 200 nm transparent indium tin oxide (ITO) electrode on the surface of the PMN-PT ceramic. Cut the ceramic into a 4 mm × 4 mm square piece and place it on a glass substrate; (3) Using the processed brass ring as the outer shell, place the square ceramic piece at the center of the brass ring. Then, connect the ITO layer and the outer shell with the positive and negative electrode wires; (4) Pour transparent epoxy resin as a backing layer into the brass ring, and bond the ceramic piece and the brass shell to form a whole; (5) After the backing layer solidifying, remove the glass substrate. In order to form a conductive closed-loop circuit, connect the ITO layer of the ceramic piece to the shell using conductive silver adhesives at the bottom of the brass ring; (6) Finally, parylene-C film with a thickness of 34 μm and 20 μm was deposited on the outer surface of TPUT using a polyp-xylene deposition system.

2.3. Photoacoustic/ultrasound dual-mode imaging system

The photoacoustic/ultrasound imaging system setup is shown in Fig. 2: The laser beam (EKSPLA, NT242, 1064 nm, 1 kHz) emitted from the laser source is coupled into an optical fiber (core diameter: 105 μm) *via* a coupled lens, collimated using an optical collimating lens, focused by an optical focusing lens and finally passes through the TPUT onto the sample. The sample generates photoacoustic signals, which are received by the transparent transducer and amplified by the ultrasound pulser/receiver (5073 PR, Olympus, Tokyo, Japan). The signals from the receiver are then acquired by a data acquisition card (ATS9371, Alazar Tech, Pointe-Claire, QC,

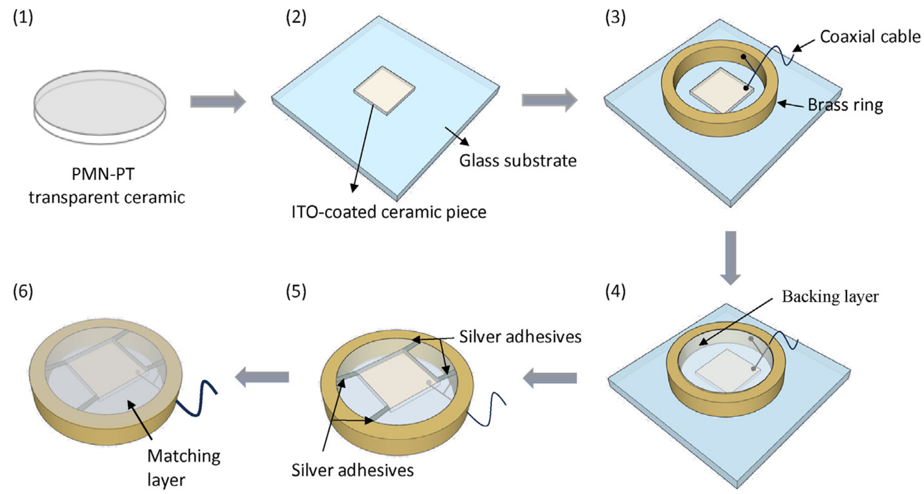

Fig. 1. Fabrication procedure of transparent piezoelectric ultrasonic transducer (TPUT). ITO: indium tin oxide.

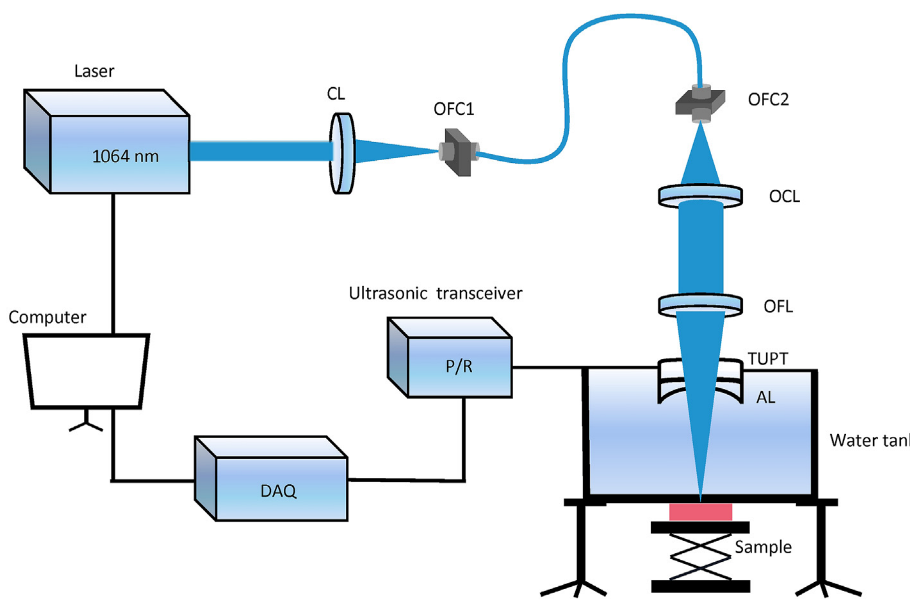

Fig. 2. A PA/US dual-modal imaging system integrated with TUPT. CL, Coupled lens; OFC, Optical fiber connector; OCL, Optical collimating lens; OFL, Optical focusing lens; AL, Acoustic lens.

Canada). The subsystem composed of optical collimating lens, optical focusing lens, TPUT, and acoustic lens (f = 24 mm) is collectively mounted on a custom-made bracket, which is connected to a two-dimensional translation stage for scanning and imaging purposes. TPUT is immersed in a water tank, and the bottom of the tank has an opening. The sample is placed below a layer of plastic wrap, which is sealed to the water tank.

2.4. Ceramic characterizations

The phase structure of the 2%Eu-PMN-28PT transparent ceramic was characterized using X-ray diffraction (D8 ADVANCE, Bruker, Germany). To test its electrical properties, the ceramic cylinder was cut into 1 mm-thick samples, and platinum was sputtered onto the sample surfaces to serve as electrodes. An electric field of 9 kV/cm was applied to the samples at room temperature in silicone oil for 20 min. The piezoelectric coefficient d_{33} was measured with a Berlincott meter (ZJ-4AN, Institute of acoustic, Chinese Academic Society, China). The ferroelectric testing system (Precision LC, Radiant Technologies, USA) was used to record the ferroelectric hysteresis (P-E) loops and strain (S-E) curves. The optical transmittance curves of polished samples were collected using a UV visible near-infrared spectrophotometer (U-4100, Hitachi, Japan). The polished sample was etched in a mixed solution of HCl and HF acids, and its microstructure was observed through a scanning electron microscope (JSM-6390LV, JEOL, Tokyo, Japan). The electromechanical coupling factors and dielectric constants were measured by an impedance analyzer (CPT2020, PolyK Technologies, USA).

The planar electromechanical coupling coefficient k_p, thickness electromechanical coupling coefficient k_t, and longitudinal electromechanical coupling coefficient k_{33} are respectively calculated according to the following equations [37]:

$$\frac{1}{k_p^2} = 0.398\frac{f_r}{f_a - f_r} + 0.579 \quad (1)$$

$$k_t^2 = \frac{\pi f_r}{2f_a}\cot\left(\frac{\pi f_r}{2f_a}\right) \quad (2)$$

$$(k_{33})^2 \approx (k_p)^2 + (k_t)^2 - (k_p)^2(k_t)^2 \quad (3)$$

Among them, f_r and f_a are the resonant frequency and anti-resonant frequency, respectively.

The dispersion coefficient γ could be calculated according to Curie Weiss law. When the temperature exceeds the Curie temperature, the dielectric temperature spectrum of relaxor ferroelectrics at low frequencies satisfies the improved Curie Weiss law [38]:

$$\frac{1}{\varepsilon} - \frac{1}{\varepsilon_m} = \frac{(T - T_m)^\gamma}{C^*} \quad (4)$$

in which C^* is the corrected Curie Weiss constant, and T is the absolute temperature, ε_m is the peak dielectric constant, T_m is the temperature of the peak dielectric constant.

2.5. TPUT characterizations

To characterize the acoustic performance of TPUT, the pulse repetition frequency and gain of the ultrasonic transmitter and receiver (5073 PR, Olympus, Japan) were set as 1 kHz and 0 dB, respectively, and the pulse echo response was measured in the mode of Fast Fourier Transform (FFT). Then, the electromechanical performance of TPUT is tested by connecting it to an impedance analyzer (4294A, Agilent Tech, Santa Clara, CA, USA). The center frequency (f_c), −6 dB bandwidth (BW) and the effective electromechanical coupling coefficient (k_{eff}) are calculated using the following formulas:

$$f_c = \frac{f_1 + f_2}{2} \quad (5)$$

$$BW = \frac{f_2 - f_1}{f_c} \quad (6)$$

$$k_{eff} = \sqrt[2]{1 - \left(\frac{f_r}{f_a}\right)^2} \quad (7)$$

Among them, f_1, f_2, f_r and f_a are the lower and upper limit frequencies of −6 dB, resonant frequency and anti-resonant frequency, respectively.

2.6. Resolution characterizations

The lateral resolution of the TPUT-based ultrasound/photoacoustic imaging system is measured using the knife-edge method. A piece of black tape fixed on a quartz plate serves as the knife edge, and a 1064 nm, 20 μJ laser pulse is used to generate the photoacoustic signal. The imaging system, driven by a motor, scanned the tape in 50 μm steps over a 3 cm range. The resolution is calculated as follows: 1. Perform a Hilbert transform on the photoacoustic/ultrasound signal waveforms to obtain their envelopes; 2. Extract the peak values of the envelopes (representing signal amplitudes) and normalize them to their maximum value; 3. Fit the data with the cumulative distribution function (CDF) to get the edge spread function (ESF); 4. Differentiate the ESF to get the line spread function (LSF); 5. Measure the full width at half maximum (FWHM) of the LSF curve to obtain the system's lateral resolution.

3. Results and discussion

3.1. Ceramic properties

As shown in Fig. 3a, the transmittance of the 2%Eu-PMN-PT ceramic exhibits a rapid increase beyond 400 nm wavelength, reaching levels as high as 68% in the visible and near-infrared regions, closely approaching the theoretical value (~71%) [39]. The characteristic absorption peak around 2000 nm corresponds to the transition of $^7F_0 \rightarrow {}^7F_6$ in Eu^{3+}. Clear visibility of both nearby and distant scenes through the 2%Eu-PMN-PT ceramic is evident, as illustrated in the inset in Fig. 3a and b, affirming its good transmittance. Fig. 3c shows the unipolar strain curve measured at 2 kV/cm and 10 Hz, with the effective piezoelectric strain coefficient d_{33}* calculated as 1890 pm/V according to the formula $d_{33}^* = S_{max}/E_{max}$ [40,41]. While the piezoelectric coefficient measured by the quasi-static d_{33} m is as high as 1500 pC/N, representing the highest reported d_{33} level of transparent piezoelectric ceramics to date [42,43]. Comparison with other transparent materials reveals that both the transparency and the d_{33} of the Eu-doped PMN-PT transparent ceramics developed in this study are comparable to ac-poled PMN-PT single crystals. The planar electromechanical coupling factor k_p, thickness electromechanical coupling k_t, and longitudinal electromechanical coupling k_{33} are respectively calculated to be 0.69, 0.65, and 0.83, based on Equations (1)–(3) and the resonant frequency f_r and anti-resonant frequency f_a measured in Fig. 4a.

Domain configuration was characterized by PFM and shown in Fig. 4b and c. Irregular watermarks domains with average width around 220 nm were observed. The random distribution of curved domain walls within watermarks domains exhibits minimal optical anisotropy. Additionally, it's worth noting that only the light with wavelengths above 400 nm (the upper limit of the absorption range, seeing Fig. 3a) is likely to permeate the ceramic, a range much larger than the average domain size (~220 nm). Thus, the incident light possesses a substantial probability of traversing the ceramic *via* successive scattering between the domains, akin to the Tyndall effect, thereby enhancing transparency [44–47]. A dense microstructure characterized by minimal pores (Fig. S1) further mitigates light scattering and enhancing transmittance.

The wavelength band at which a material can be transparent depends on its band gap width E_g Ref. [48]. For PMN-PT, selecting an appropriate crystal phase to reduce light birefringence and suppressing light scattering through microstructure engineering (ensuring density, minimizing pores, and optimizing grain size and domain size) can result in transparency at wavelengths above 400 nm (depending on E_g). Defects and oxygen vacancies, on the other hand, can form color centers that result in light absorption. The ceramics in this work were prepared by a two-step sintering process including oxygen sintering. The transmittance of the obtained ceramics is close to the theoretical transmittance, with the only notable absorption peak arising from the characteristic absorption of Eu^{3+}, while no obvious light absorption from color centers relating to defects or oxygen vacancies was observed.

The small-size domain may originate from the disruption of the long-range order arrangement of A-site ions by Eu doping. Consequently, relaxation characteristics appear to be reinforced, as evidenced by the distinct frequency dispersion in dielectric spectrum (Fig. 4d) and the large dispersion coefficient γ ~1.86 (calculated by Equation (4), Figs. 4e and 1 < γ < 2, $\gamma = 1$ meaning normal ferroelectrics and $\gamma = 2$ meaning complete relaxor). In addition, easy domain switching can be expected due to the small coercive electric field (only ~3 kV/cm, Fig. 4f). It is interesting to note a good rectangularity (the squareness R_{sq} is calculated as 1.27, $R_{sq} = P_r/P_s + P_{1.1Ec}/P_r$, where P_s is the spontaneous polarization and $P_{1.1Ec}$ is

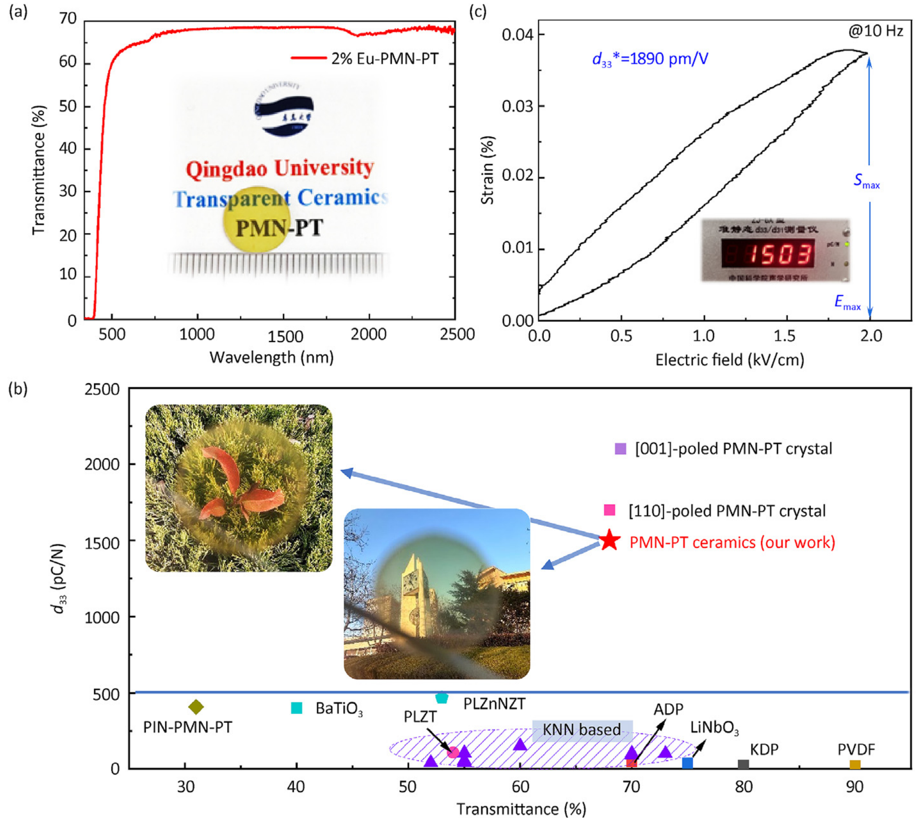

Fig. 3. Optical transmittance and piezoelectric properties. (a) Transmission spectrum and photograph (inset) of a 2%Eu-PMN-PT transparent ceramic with thickness of 0.4 mm; (b) Comparison of the transmittance and piezoelectric coefficient with actively studied transparent piezoelectric materials. The two insets are photos of nearby scenery and distant scenery through the transparent ceramic; (c) Unipolar strain curve measured at 10 Hz and 2 kV/cm. The inset displays the piezoelectric coefficient measured by the quasi-static d_{33} m.

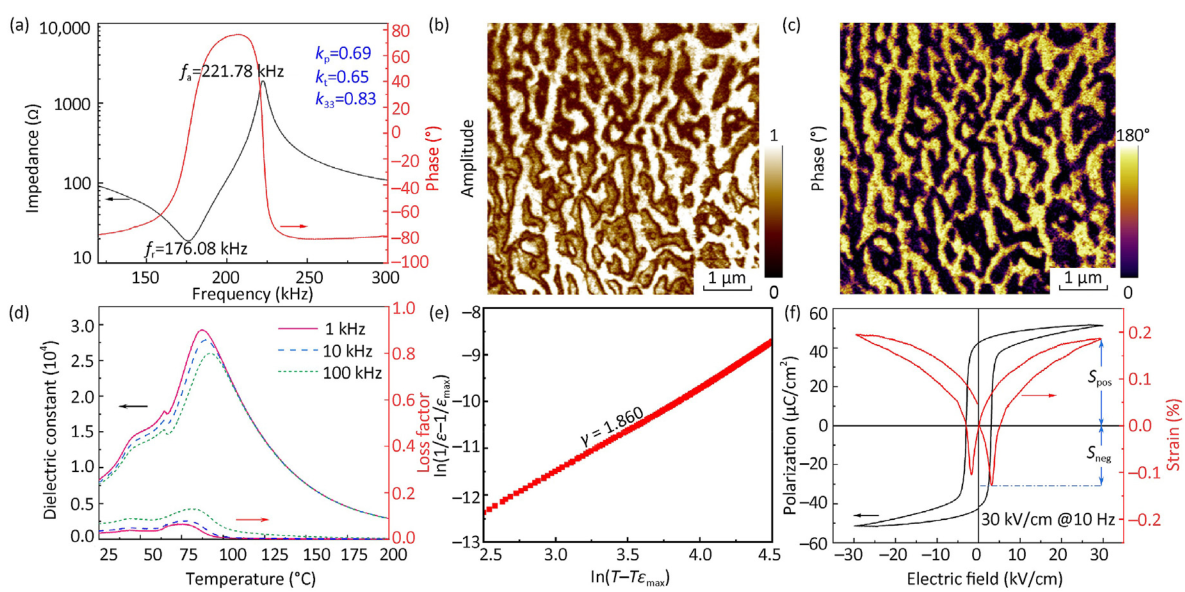

Fig. 4. Piezoelectric, ferroelectric, dielectric performance and microstructure of 2%Eu-PMN-28PT ceramic. (a) Impedance and phase diagram. (b) Amplitude image and (c) phase image of the domain configuration revealed by piezoelectric force microscopy (PFM). (d) The dependence of dielectric constant and loss on temperature at different frequencies, measured in poled sample. (e) The plots of ln $\left(\frac{1}{\varepsilon}-\frac{1}{\varepsilon_{\max}}\right)$ *versus* ln $(T-T_{\varepsilon_{\max}})$. (f) Ferroelectric hysteresis loop and bipolar strain curve measured at 10 Hz and 30 kV/cm.

the polarization at electric field of 1.1 times the coercive field) exists in ferroelectric hysteresis loop accompanied by a high remnant polarization (P_r ~ 42 μC/cm^2, Fig. 4f), attributed to the introduction of local tetragonal phase by Eu doping, as indicated by the slightly split (111) and (200) XRD peaks (Fig. S2). All these are responsible for the observed superior piezoelectric properties.

Notably, as seen in the bipolar strain curve in Fig. 4f, the positive strain S_{pos} (the difference between the maximum strain and the zero electric field strain) reaches 0.186%, comparable with the value (~0.199%) in unipolar strain curve at 30 kV/cm. While the negative strain S_{neg} (the difference between the minimum strain and the zero electric field strain) is −0.127% Typically, S_{neg} can represent the contribution to piezoelectric properties from the irreversible non-180° domain switching, just like the remnant strain that measured through the first bipolar cycle in an unpoled sample [49–54]. Moreover, if the sample is poled sufficiently, the unipolar strain

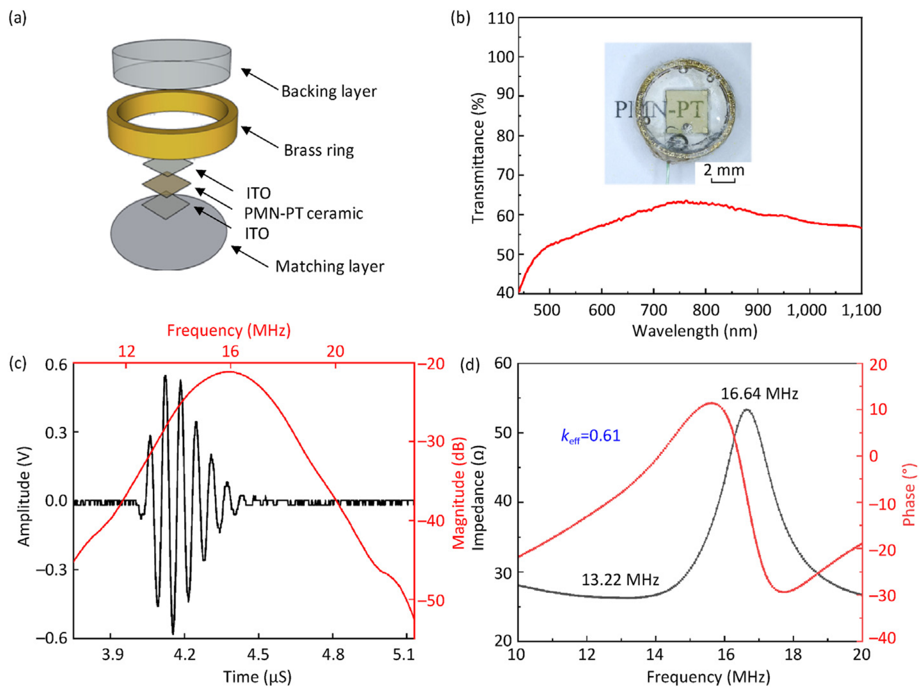

Fig. 5. TPUT properties. (a) Exploded view of TPUT. ITO: indium tin oxide. Ceramic thickness ~150 µm. (b) Transmittance spectrum and photograph of TPUT. Pulse-echo response, frequency spectrum (c) and impedance-phase diagram (d) of the TPUT.

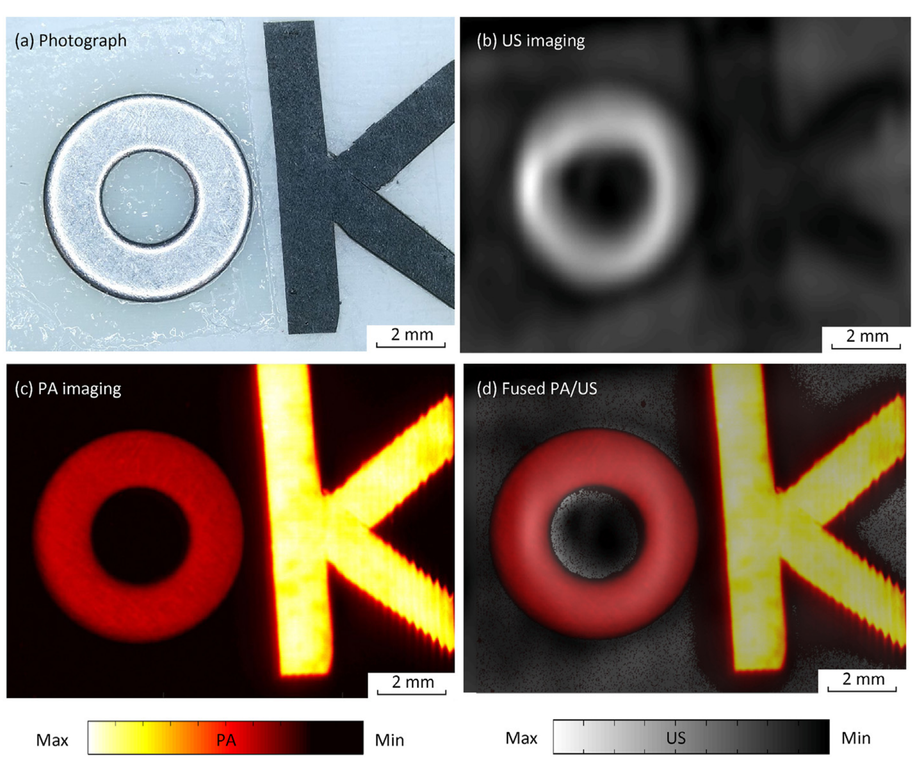

Fig. 6. PA/US Dual-Mode Imaging of the "OK". "O" is a metal ring; "K" is made of black tapes; the base plate is resin. (a) Photograph. (b) US imaging. US: ultrasound. (c) PA imaging. PA: photoacoustic. (d) Fused PA/US imaging of the word "OK". Max: maximum; Min: minimum.

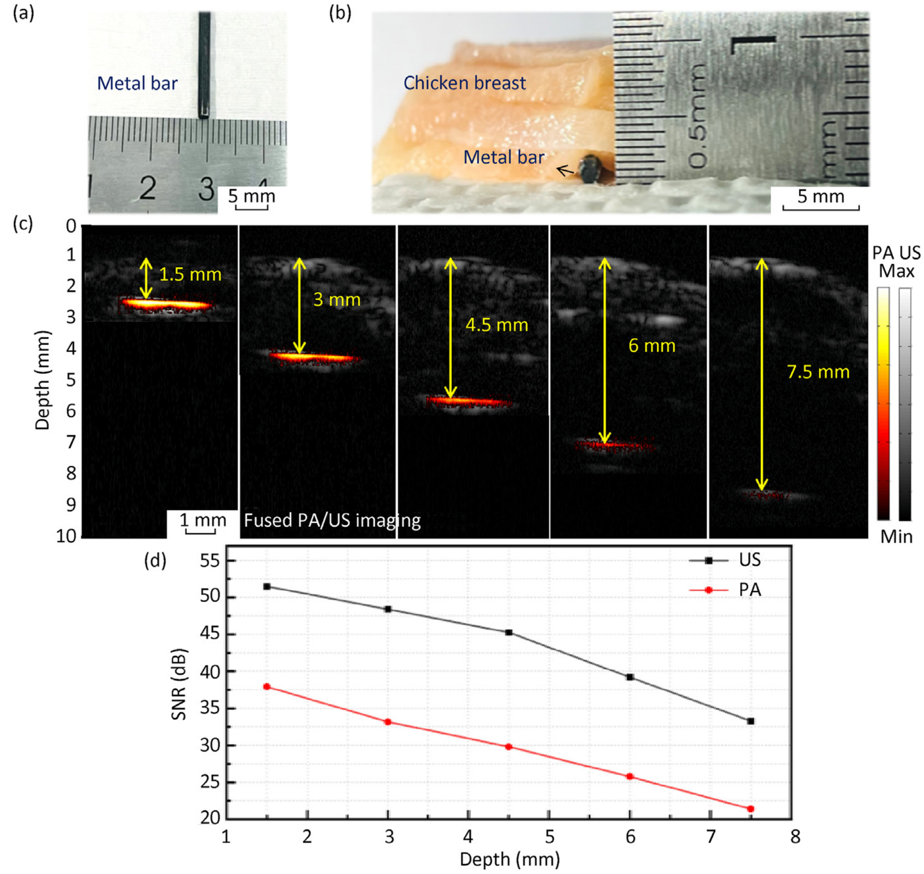

Fig. 7. PA/US signal detection of deep tissues *in vitro*. (a) Detection target: Metal bar. (b) Placement of the metal bar beneath few slices of chicken breast meat. There is glue between the chicken breast slices. (c) Fused PA/US imaging of metal bar beneath different thicknesses of chicken breast meat. (d) Change of the signal-to-noise ratio (SNR) of PA/US imaging of metal bar with different thicknesses of chicken breast meat. The wavelength of the laser used in the experiment is 1064 nm, and the energy of the laser passing through TPUT is 45 μJ.

Table 1
Comparison of PA imaging depth and SNR with other ultrasonic transducers.

Ultrasonic transducers		f_c (MHz)	Wavelength (nm)	Light energy (μJ)	Imaging depth (mm)	SNR (dB)	Reference
Opaque	Commercial UT	50	559–576	NA	4.6	2.5	[56]
					7.6	1.4	
Transparent	PVDF film	36	532	35	1	36.5	[13]
					3	22	
	$LiNbO_3$ crystal	13	532	19	NA	38	[57]
	PMN-PT crystal	8	650	NA	0	33	[58]
					3	27	
	Eu-PMN-PT ceramic	16	1064	45	1.5	38	This work
					7.5	21	

S_{total} simply comes from the remnant irreversible non-180° domain switching (being approximate to S_{neg}), the reversible field-induced domain switching and the reversible field-induced lattice distortion. Thus, the extrinsic contribution to the piezoelectric properties from the irreversible domain switching can be estimated by S_{neg}/S_{total}, which is 64% in our 2%Eu-PMN-28PT transparent ceramics.

3.2. The fabrication and properties of TPUT

The structure of TPUT based on PMN-PT transparent ceramic is illustrated by the exploded view in Fig. 5a. Except for the copper ring, all materials used in TPUT are transparent. A photograph of finished TPUT can be found in Fig. 5b, showing good transmittances in the visible and near-infrared regions. In our photoacoustic imaging (PAI) experiment, the transmittance of TPUT at operating wavelength of ~1064 nm reaches 57%. As commonly known, the center frequency of the transducer is determined by the thickness of the piezoelectric material, resulting in a center frequency of 16 MHz for the TPUT with ceramic thickness ~150 μm, as depicted in the frequency spectrum in Fig. 5c shown. In addition, the center frequency of the TPUT closely aligns with the anti-resonant frequency observed in the impedance spectrum (Fig. 5d). According to Equation (6), the −6 dB bandwidth of TPUT is 30%, accompanied by a pulse-echo amplitude as high as 1.12 V. Notably, according to the impedance phase diagram in Fig. 5d and Equation (7), the effective electromechanical coupling factor k_{eff} is calculated to be as high as 0.61, surpassing that of TPUT based on LN crystals and comparable to TPUT based on PMN-PT crystals [16,18,25,55].

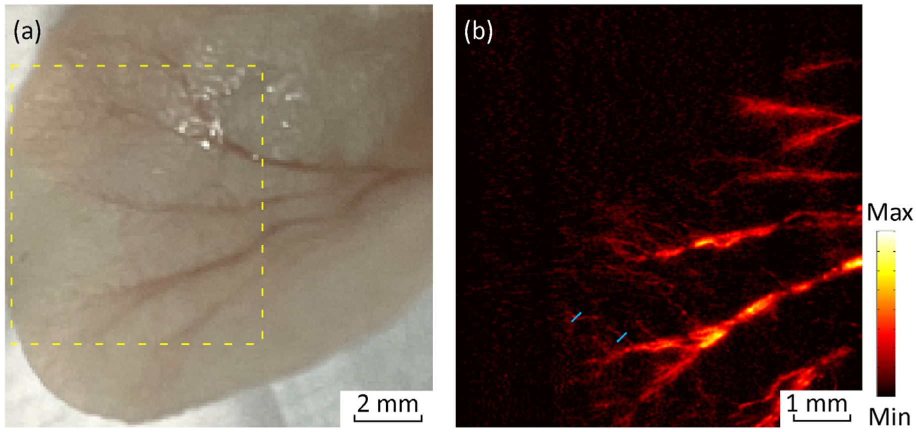

Fig. 8. PA imaging of the subcutaneous microvasculature network in a mouse ear. (a) Photo of the mouse ear. (b) PA image of the subcutaneous microvasculature network imaging from the rectangular area of (a).

3.3. PA/US dual-mode imaging

The resolution of US/PA imaging system based on TPUT was tested, as shown in Fig. S3. The lateral resolutions, *i.e.*, the FWHM in Fig. S3, for US and PA, are 320 μm and 225 μm, respectively. There are two main reasons contributing to the subpar lateral resolution: Firstly, the focus on achieving large depth compromises the attainment of high lateral resolution; Secondly, additional optimization of optical pathway system is necessary.

Subsequently, the US/PA dual mode imaging was applied on composite objects, involving a metal ring and black tapes arranged to form shapes of letters “O” and “K” (Fig. 6a). US imaging is mainly relying on sound wave reflection caused by the different acoustic impedance between tissues, thus highlighting the structural information of tissues and commonly used to evaluate the structure uniformity of tissues. Evidently, the difference in acoustic impendence between metal (~40 MRayl) and water medium (~1.5 MRayl) is significantly larger than that between black tape (~3 MRayl) and water. Renowned for its sensitivity to acoustic impedance disparities, the US imaging reveals the high echogenicity of the metal “O” and the low echogenicity of the black tape “K” compared to the reference resin, as clearly demonstrated in Fig. 6b. Obviously, there is material inhomogeneity in the metal “O”, which can be witnessed from the uneven brightness of its US image.

In contrast, PA imaging is based on the distinct absorption characteristics of different tissues. Therefore, it can provide excellent imaging contrast and functional information about tissues. Simultaneously, within the same area, we obtain a PA image of the “OK” letters (Fig. 6c), which is much clearer than the corresponding US image. It is observed that the PA signal from “K” significantly surpasses “O” due to the higher optical absorption of the black tape, with both showing good uniformity due to the homogeneity of “OK” surface. Fig. 6d is the fused PA/US image, seamlessly integrating the PA signal generated from optical absorption and the US signal from the ultrasound reflection. PA/US dual-mode imaging simultaneously highlights both structural and functional information of the two letters, involving internal structure inhomogeneity and surface material uniformity. Due to the evident superiority of the PA/US imaging, dual-mode technology has found widespread use in disease diagnosis and holds great potential in biomedical application.

3.4. In vitro and deep tissue PA/US imaging

To explore the sensitivity of TPUT, we conducted in vitro and deep tissue PA/US signal detection experiments, as illustrated in Fig. 7 Chicken breast meat serves as the attenuation layer for optical and acoustic penetration, with a metal bar of 2 mm diameter is used as the signal detection target (Fig. 7a). Sequentially, five pieces of chicken breast meat were placed atop the metal bar, with the thickness of tissues changing from 1.5 mm to 7.5 mm (Fig. 7b). The PA/US imaging of the metal bar beneath different thickness of chicken meat was conducted and displayed in Fig. 7c, with PA imaging clearly exhibiting superior contrast and resolution compared to US imaging. The corresponding SNR of PA and US signals were quantitatively analyzed (Fig. 7d). Given the metal bar's large acoustic impedance and minimal optical absorption coefficient, the SNR of its US signal is generally higher than that of the PA signal. With the increase in chicken breast thickness, the SNR of PA and US decreased simultaneously. At a 1.5 mm thickness chicken breast, the SNR of US remained at 53 dB, while PA was 38 dB. Notably, as the stacked layers reached a thickness of 7.5 mm, the SNR still maintained relatively high at 33 dB and 21 dB for US and PA respectively. Although comparison with other transducers about the imaging depth are challenging due to the differences in center frequencies, light wavelengths, and energy level, as listed in Table 1, it is noteworthy that at a center frequency of 16 MHz and the input laser energy of 45 μJ, the SNR for PA imaging through 7.5 mm tissue still maintained at 21 dB, representing a commendable performance.

3.5. In-vivo PA imaging

To validate the *in vivo* imaging capability of our TPUT, we carried out PA imaging of the subcutaneous microvasculature network in a mouse ear. A 532 nm pulsed laser was used to excite the PA signals from the hemoglobin in red blood cells, while a TPUT with a center frequency of 28 MHz was selected to image the capillary vessels. The properties of this high-frequency TPUT are given in Fig. S4, in which the −6 dB bandwidth reaching 30%. We replaced the 105 μm fiber in the imaging optical path with a 9 μm fiber to obtain a smaller spot and removed the acoustic lens to reduce the imaging distance. The resulting PA image of the subcutaneous microvasculature network in a mouse ear (Fig. 8a) is displayed in Fig. 8b. In addition to some main thick blood vessels, the PA signals of many capillaries were also detected, demonstrating the good resolution and sensitivity of the studied TPUT based on 2% Eu-PMN-28PT ceramic in in-vivo PA imaging.

4. Conclusions

In this work, we prepared highly transparent PMN-PT ceramics with *T*~ 68% in the visible and near-infrared regions, nearing its theoretical transmittance limit of ~71%. Additionally, these ceramics exhibited an ultrahigh d_{33} reaching as high as 1500 pC/N, marking the highest documented d_{33} values in transparent piezoelectric ceramics to date. This outstanding performance is attributed to a combination of factors, including the refined domain structure, easy domain switching and the introduction of tetragonal local structure heterogeneities. Leveraging the PMN-PT transparent ceramic, we have successfully developed a high sensitivity transparent piezoelectric ultrasonic transducer (TPUT). The TPUT features adjustable frequency and bandwidth, while maintaining substantial transmittance under imaging light. Through PA/US dual-mode imaging, we validated its capability to capture both functional and structural information, showcasing superior performance in deep tissue imaging. Additionally, the TPUT exhibited good capabilities of *in-vivo* PA imaging. Overall, our study highlights the efficacy of PMN-PT transparent piezoelectric ceramics in advancing cost-effective biomedical photoacoustic imaging with TPUT technology.

CRediT authorship contribution statement

Pengkun Guo: Writing – original draft, Formal analysis, Data curation. **Wen Gao:** Data curation. **Riqiang Lin:** Methodology, Formal analysis. **Xiatian Wang:** Data curation. **Jiale Lan:** Software. **Jiaming Zhang:** Data curation. **Yanan Wang:** Data curation. **Lin Zhu:** Data curation. **Yongcheng Zhang:** Formal analysis. **Feng Li:** Data curation. **Weijie Zheng:** Data curation. **Tianlong Zhao:** Data curation. **Kwok-Ho Lam:** Data curation. **Xiaojing Gong:** Methodology, Data curation. **Zhihua Xie:** Writing – review & editing, Methodology, Formal analysis. **Yalin Qin:** Writing – review & editing, Supervision, Methodology. **Shujun Zhang:** Writing – review & editing, Supervision, Formal analysis.

Declaration of competing interest

The authors declare that they have no known competing financial interests or personal relationships that could have appeared to influence the work reported in this paper.

Acknowledgements

This work was financially supported by the National Natural Science Foundation of China (Grant Nos. 11604171 and 52272116), the Youth Innovation Team Project of Shandong Provincial Education Department (2019KJJ012), Natural Science Foundation of Guangdong Province (2022A1515110771), Shenzhen Engineering Laboratory for Diagnosis & Treatment Key Technologies of Interventional Surgical Robots (XMHT20220104009), and the Shenzhen Science and Technology Innovation Committee (ZDSY20130401165820357, JCYJ20220818101417039, JCYJ20210324101612034, JCYJ2020010 9114610201). The author Y. Qin thanks the support by Key Laboratory of Biomedical Imaging Science and System, Chinese Academy of Sciences.

Appendix B. Supplementary data

Supplementary data to this article can be found online at https://doi.org/10.1016/j.jmat.2024.100932.

References

[1] Wang L, Hu S. Photoacoustic tomography: *in vivo* imaging from organelles to organs. Science 2012;335(6075):1458–62.
[2] Yao J, Wang L. Photoacoustic microscopy. Laser Photon Rev 2013;7(5): 758–78.
[3] Du W, Suh E, Lin D, Marcus C, Ozkan L, Dagdeviren C, et al. Conformable ultrasound breast patch for deep tissue scanning and imaging. Sci Adv 2023;9(30):eadh5325.
[4] Zhang L, Marcus C, Lin D, Mejorado D, Schoen S, Pierce T, et al. A conformable phased-array ultrasound patch for bladder volume monitoring. Nat Electron 2023;7(1):77–90.
[5] Maslov K, Zhang H, Hu S, Wang L. Optical-resolution photoacoustic microscopy for in vivo imaging of single capillaries. Opt Lett 2008;33(9):929–31.
[6] Hu S, Maslov K, Wang L. Second-generation optical-resolution photoacoustic microscopy with improved sensitivity and speed. Opt Lett 2011;36(7): 1134–6.
[7] Wang H, Yang X, Liu Y, Jiang B, Luo Q. Reflection-mode optical-resolution photoacoustic microscopy based on a reflective objective. Opt Express 2013;21(20):24210–8.
[8] Wang L, Maslov K, Wang L. Single-cell label-free photoacoustic flowoxigraphy in vivo. Proc Natl Acad Sci USA 2013;110(15):5759–64.
[9] Yao J, Wang L, Li C, Zhang C, Wang L. Photoimprint photoacoustic microscopy for three-dimensional label-free subdiffraction imaging. Phys Rev Lett 2014;112(1):014302.
[10] Tang Y, Liu W, Li Y, Zhou Q, Yao J. Concurrent photoacoustic and ultrasound microscopy with a coaxial dual-element ultrasonic transducer. Vis Comput Ind Biomed Art 2018;1(1):3.
[11] Fang C, Hu H, Zou J. A focused optically transparent PVDF transducer for photoacoustic microscopy. IEEE Sensor J 2020;20(5):2313–9.
[12] Park J, Park B, Kim T, Lee D, Yong U, Jang J, et al. Seamlessly integrated optical and acoustical imaging systems through transparent ultrasonic transducer. Photons Plus Ultrasound: Imaging and Sensing 2020;11240:69–74.
[13] Fang C, Zou J. Acoustic-resolution photoacoustic microscopy based on an optically transparent focused transducer with a high numerical aperture. Opt Lett 2021;46(13):3280–3.
[14] Park B, Kim H, Kim C. Versatile optical and ultrasound imaging platforms using transparent ultrasound transducers. Opt spectrosc. Optica Publishing Group; 2022. p. 2.
[15] Niederhauser J, Jaeger M, Hejazi M, Keppner H, Frenz M. Transparent ITO coated PVDF transducer for optoacoustic depth profiling. Opt Commun 2005;253(4–6):401–6.
[16] Park J, Park B, Kim T, Jung S, Choi W, Ahn J, et al. Quadruple ultrasound, photoacoustic, optical coherence, and fluorescence fusion imaging with a transparent ultrasound transducer. Proc Natl Acad Sci USA 2021;118(11): e1920879118.
[17] Liu Y, Kurnikov A, Li W, Kazakov V, Ni R, Subochev P, et al. Sensitive ultra-wideband transparent PVDF-ITO ultrasound detector for optoacoustic microscopy. Opt Lett 2022;47(16):4163–6.
[18] Brodie G, Qiu Y, Cochran S, Spalding G, MacDonald M. Optically transparent piezoelectric transducer for ultrasonic particle manipulation. IEEE Trans Ultrason Ferroelectrics Freq Control 2014;61(3):389–91.
[19] Dangi A, Agrawal S, Kothapalli S. Lithium niobate-based transparent ultrasound transducers for photoacoustic imaging. Opt Lett 2019;44(21):5326–9.
[20] Blumenrother E, Melchert O, Kanngiesser J, Wollweber M, Roth B. Single transparent piezoelectric detector for optoacoustic sensing-design and signal processing. Sensors 2019;19(9):2195.
[21] Bao H, Ma Y, Sun J, Zhao Q, Yang L, Hou Y, et al. Flexible and transparent ionic liquids/poly(vinylidene fluoride) composition-gradient piezo-active composites for highly sensitive pressure sensor. Adv Electron Mater 2022;9(2): 2201013.
[22] Thalhammer G, McDougall C, MacDonald M, Ritsch-Marte M. Acoustic force mapping in a hybrid acoustic-optical micromanipulation device supporting high resolution optical imaging. Lab Chip 2016;16(8):1523–32.
[23] Qiu C, Wang B, Zhang N, Zhang S, Liu J, Walker D, et al. Transparent ferroelectric crystals with ultrahigh piezoelectricity. Nature 2020;577(7790): 350–4.
[24] Li F, Qiu C, Zhang Z, Xu Z, Qiao L, Zhang S, et al. Transparent ultrasonic transducers based on relaxor ferroelectric crystals for advanced photoacoustic imaging. Nat Commun 2024;15:10580.
[25] Chen H, Mirg S, Osman M, Agrawal S, Cai J, Biskowitz R, et al. A high sensitivity transparent ultrasound transducer based on PMN-PT for ultrasound and photoacoustic imaging. IEEE Sens Lett 2021;5(11):1–4.

[26] Zhao X, Chao X, Wu D, Liang P, Yang Z. Simultaneous realization of high transparency and piezoelectricity in low symmetry KNN-based ceramics. J Am Ceram Soc 2018;102(6):3498. 09.
[27] Ren X, Peng Z, Chen B, Shi Q, Qiao X, Wu D, et al. A compromise between piezoelectricity and transparency in KNN-based ceramics: the dual functions of Li_2O addition. J Eur Ceram Soc 2020;40(6):2331–7.
[28] Lin J, Wang Y, Xiong R, Sa B, Shi C, Zhai J, et al. Tailoring micro-structure of eco-friendly temperature-insensitive transparent ceramics achieving superior piezoelectricity. Acta Mater 2022;235:118061.
[29] Rojac T, Ursic H, Bencan A, Malic B, Damjanovic D. Mobile domain walls as a bridge between nanoscale conductivity and macroscopic electromechanical response. Adv Funct Mater 2015;25(14):2099–108.
[30] Otoničar M, Bradeško A, Fulanović L, Kos T, Uršič H, Benčan A, et al. Connecting the multiscale structure with macroscopic response of relaxor ferroelectrics. Adv Funct Mater 2020;30(52):2006823.
[31] Zhang L, Wang D, Guo M, Lou X, Wang D. A new strategy for large dynamic piezoelectric responses in lead-free ferroelectrics: the relaxor/morphotropic phase boundary crossover. Adv Funct Mater 2020;30(45):2004641.
[32] Mantri S, Daniels J. Domain walls in ferroelectrics. J Am Ceram Soc 2021;104(4):1619–32.
[33] Xing J, Jiang L, Zhao C, Tan Z, Xu Q, Wu J, et al. Potassium sodium niobate based lead-free ceramic for high-frequency ultrasound transducer applications. J Materiomics 2020;6(3):513–22.
[34] Yan K, Chen X, Wang F, Zhu K. Large piezoelectricity and high transparency in fine-grained $BaTiO_3$ ceramics. Appl Phys Lett 2020;116(8):082902.
[35] Yan P, Qin Y, Xu Z, Han F, Wang Y, Wen Z, et al. Highly transparent Eu-doped 0.72pmn-0.28pt ceramics with excellent piezoelectricity. ACS Appl Mater Interfaces 2021;13(45):54210–6.
[36] Zhang Y, Song Z, Lv M, Yang B, Wang L, Chen C, et al. Comparison of PMN-PT transparent ceramics processed by three different sintering methods. J Mater Sci Mater Electron 2017;28:15612–7.
[37] Wang P, Guo Q, Li F, Xia F, Hao H, Sun H, et al. Modified $Pb(Mg_{1/3}Nb_{2/3})O_3$-$PbZrO_3$-$PbTiO_3$ ceramics with high piezoelectricity and temperature stability. J Am Ceram Soc 2021;104(10):5127–37.
[38] Bokov A, Ye Z. Recent progress in relaxor ferroelectrics with perovskite structure. J Mater Sci 2006;41:31–52.
[39] Ruan W, Li G, Zeng J, Bian J, Kamzina L, Zeng H, et al. Large electro-optic effect in La-doped $0.75Pb(Mg_{1/3}Nb_{2/3})O_3$-$0.25PbTiO_3$ transparent ceramic by two-stage sintering. J Am Ceram Soc 2010;93(8):2128–31.
[40] Kungl H, Fett T, Wagner S, Hoffmann M. Nonlinearity of strain and strain hysteresis in morphotropic LaSr-doped lead zirconate titanate under unipolar cycling with high electric fields. J Appl Phys 2007;101(4):044101.
[41] Wang B, Hong J, Yang Y, Zhao H, Long L, Zheng L. Achievement of a giant piezoelectric coefficient and piezoelectric voltage coefficient through plastic molecular-based ferroelectric materials. Matter 2022;5(4):1296–304.
[42] Li F, Lin D, Chen Z, Cheng Z, Wang J, Li C, et al. Ultrahigh piezoelectricity in ferroelectric ceramics by design. Nat Mater 2018;17(4):349–54.
[43] Guo Q, Li F, Xia F, Gao X, Wang P, Hao H, et al. High-performance Sm-doped $Pb(Mg_{1/3}Nb_{2/3})O_3$-$PbZrO_3$-$PbTiO_3$ based piezoceramics. ACS Appl Mater Interfaces 2019;11(46):43359–67.
[44] Ruan W, Li G, Zeng J, Kamzina L, Zeng H, Zhao K, et al. Origin of the giant electro-optic Kerr effect in La-doped 75PMN-25PT transparent ceramics. J Appl Phys 2011;110(7):074109.
[45] Li G, Ruan W, Zeng J, Zeng H, Zheng L, Kamzina L, et al. The effect of domain structures on the transparency of PMN-PT Transparent Ceramics. Opt Mater 2013;35(4):722–6.
[46] Zeng J, Li G, Ruan W, Zheng L, Zeng H, Ding A, et al. The influence of domain structure on the optical and electrical properties of transparent $(Pb,La)(Mg_{1/3}Nb_{2/3})O_3$-$PbTiO_3$ ceramics. Ceram Int 2013;39:S31–4.
[47] Qin Y, Yan P, Han F, Zhang Y, Lv Z, Zhou C. The piezoelectric properties of transparent $0.75Pb(Mg_{1/3}Nb_{2/3})O_3$-$0.25PbTiO_3$:$Pr^{3+}$ ceramics. J Alloys Compd 2022;891:161959.
[48] Wang Y, Guo P, Wang Y, Huo N, Sun R, Zhang Y, et al. Enhancement of the photoluminescence modulation ratio in highly transparent KNN-based ceramics for optical information storage. J Mater Chem C 2023;11(14):4775–83.
[49] Kungl H, Theissmann R, Knapp M, Baehtz C, Fuess H, Wagner S, et al. Estimation of strain from piezoelectric effect and domain switching in morphotropic PZT by combined analysis of macroscopic strain measurements and synchrotron X-ray data. Acta Mater 2007;55(6):1849–61.
[50] Fu J, Zuo R. Giant electrostrains accompanying the evolution of a relaxor behavior in $Bi(Mg,Ti)O_3$-$PbZrO_3$-$PbTiO_3$ ferroelectric ceramics. Acta Mater 2013;61(10):3687–94.
[51] Qin Y, Zhang J, Yao W, Lu C, Zhang S. Domain configuration and thermal stability of $(K_{0.48}Na_{0.52})(Nb_{0.96}Sb_{0.04})O_3$-$Bi_{0.50}(Na_{0.82}K_{0.18})_{0.50}ZrO_3$ piezoceramics with high d_{33} coefficient. ACS Appl Mater Interfaces 2016;8(11):7257–65.
[52] Huang Y, Zhang L, Shi W, Hu Q, Shur V, Wei X, et al. Ferroelectric-to-relaxor transition and ultrahigh electrostrictive effect in Sm^{3+}-doped $Pb(Mg_{1/3}Nb_{2/3})O_3$-$PbTiO_3$ ferroelectrics ceramics. J Mater Sci Technol 2023;165:75–84.
[53] Yang Y, Sun E, Xu Z, Zheng H, Yang B, Zhang R, et al. Sm and Mn co-doped PMN-PT piezoelectric ceramics: defect engineering strategy to achieve large d_{33} and high Q_m. J Mater Sci Technol 2023;137:143–51.
[54] Guo Q, Li F, Xia F, Wang P, Gao X, Hao H, et al. Piezoelectric ceramics with high piezoelectricity and broad temperature usage range. J Materiomics 2021;7(4):683–92.
[55] Chen R, He Y, Shi J, Yung C, Hwang J, Wang L, et al. Transparent high-frequency ultrasonic transducer for photoacoustic microscopy application. IEEE Trans Ultrason Ferroelectrics Freq Control 2020;67(9):1848–53.
[56] Moothanchery M, Pramanik M. Performance characterization of a switchable acoustic resolution and optical resolution photoacoustic microscopy system. Sensors 2017;17(2):357.
[57] Chen H, Agrawal S, Dangi A, Wible C, Osman M, Abune L, et al. Optical-resolution photoacoustic microscopy using transparent ultrasound transducer. Sensors 2019;19(24):5470.
[58] Park B, Han M, Park J, Kim T, Ryu H, Seo Y, et al. A photoacoustic finder fully integrated with a solid-state dye laser and transparent ultrasound transducer. Photoacoustics 2021;23:100290.

Pengkun Guo graduated from Qingdao University with a master's degree in 2024, and his main research interests are in the preparation of functional ceramics and ultrasonic transducers; currently he is mainly engaged in the direction of hydroacoustic transducers.

Wen Gao received her Master's degree from Qingdao University in 2024, where her research focused on the preparation and application of transparent ferroelectric functional ceramics. Since Aug 2022, she has been a visiting student of Shenzhen Institutes of Advanced Technology, Chinese Academy of Science. Now her current research interests on the fabrication of ultrasound transducers and endoscopic catheters for photoacoustic imaging.

Riqiang Lin received his Ph.D. degree from The Hong Kong Polytechnic University. He has been worked at the Shenzhen Institutes of Advanced Technology, Chinese Academy of Sciences over 13 years. Now he is a senior engineer and he focuses on the research of ultrasound transducer technology and photoacoustic endoscopy imaging. His current research interests focus on developing novel transparent ultrasound transducer and the photoacoustic endoscopic catheter for clinical translation.

Yalin Qin received her Ph.D. degree from Shandong University (CN) in 2015, and now works in Qingdao University (CN). She is a visiting scholar of Pennsylvania State University, member of Editorial Board of Crystals, senior member of China Instrument Functional Materials Society, member of Shandong Institute of Electronics, and member of Shandong Silicate Society. Her research interests mainly focus on the preparation, characterization, and application of transparent ferroelectric, piezoelectric, and luminescent functional ceramics.

Zhihua Xie is an Associate Professor at Shenzhen Institute of Technology, Chinese Academy of science. She received her Ph.D. degree from the University of Frache-Comte, France, 2016. Dr. Xie's research focuses on the development of micro and nano optical elements, the improvement of the photoacoustic endoscopic imaging systems and the applications of photoacoustic endoscopies.

Xiaojing Gong is a professor at Shenzhen Institutes of Advanced Technology, Chinese Academy of Sciences. He received B.S. degree in Mechatronics from the Southeast University in 2000, and Ph.D. degree in Fine Instruments and Mechanics from the University of Science and Technology of China in 2007. His interest focuses on multimodality endoscopic imaging development and research (including photoacoustic imaging, optical coherent tomography, and ultrasonic imaging) and its clinical translation, such as intravascular imaging, gastrointestinal endoscopy, and reproductive tract endoscopy.